Crowning lithium ions in hole transport layer toward stable perovskite solar cells

Ying Shen
  Soochow University

Kaimo Deng
  Soochow University

Qinghua Chen
  Soochow University

Gui Gao
  Soochow University

liang li (✉ lli@suda.edu.cn)
  Soochow University

Article

Keywords:

Abstract

State-of-art perovskite solar cells exhibit comparable power conversion efficiency to silicon photovoltaics. However, the device stability remains a major obstacle that restricts widespread application. Doping hole transport layer induced hygroscopicity, ion diffusion, and use of polar solvent are detrimental factors for performance degradation of perovskite solar cells. Here, we report phase transfer catalyzed LiTFSI doping in Spiro-OMeTAD to address these negative impacts. 12-crown-4 as an efficient phase transfer catalyst promotes the dissolution of LiTFSI without requiring acetonitrile. Crowning Li^+ ions by forming more stable and less diffusive crown ether-Li^+ complexes retards the generation of hygroscopic lithium oxides and mitigates Li^+ ion migration. Optimized solar cells deliver enhanced power conversion efficiency and significantly improved stability under humid and thermal conditions compared with the control device. This method can also be applied to dope π-conjugated polymer. Our findings provide a facile avenue to improve the long-term stability of perovskite solar cells.

Introduction

Despite an encouraging power conversion efficiency (PCE) exceeding 25% for state-of-art perovskite solar cells (PSCs) being sufficient for practical applications,[1−6] a huge concern over the device stability remains to be addressed. Except for the vulnerability of perovskite layers toward ambient conditions,[7] the most frequently used small-molecule hole transporting layer (HTL) for highly efficient PSCs, Spiro-OMeTAD [2,2',7,7'tetrakis(N,N-di-p-methoxyphenylamine)-9,9'-spirobi-fluorene], shows a poor stability toward humid and thermal conditions. Limited by an intrinsically low mobility of pristine Spiro-OMeTAD, LiTFSI [bis(trifluoromethanesulfonyl)imide] must be added as a p-type dopant to increase the conductivity.[8] LiTFSI, however, has low solubility in chlorobenzene (CB), the solvent for dissolving Spiro-MeOTAD. It is usually pre-dissolved in a polar solvent, typically acetonitrile.[9] The instability of Spiro-MeOTAD mainly arises from the indispensable dopants. On the one hand, the metal halide perovskite are vulnerable to polar solvent and it is desired to avoid or reduce the use of acetonitrile.[10] On the other hand, the hygroscopic lithium salt facilitates moisture penetration and Li^+ ion migration that is accelerated under high temperature conditions induces lithium intercalation into the perovskite layer with the formation of deleterious defects.[11]

Thus far, considerable efforts have been devoted to optimizing the HTL of PSCs for enhanced PCE and stability.[12−14] The research community is actively searching for equivalent substitutes[15−18] to Spiro-OMeTAD for simple synthesis and cost reduction. Notwithstanding the recent success, LiTFSI is essential to these newly synthesized HTLs and Spiro-OMeTAD still represents the best choice for PSCs at the current stage owing to its high compatibility with dopants and energy band matching with perovskite.[19,20] Toward Spiro-OMeTAD based HTL, alternative dopants instead of LiTFSI such as Spiro(TFSI)$_2$,[21] lithium-ion endohedral fullerene,[22] and lithium-ion-free salts[23,24] have been studied to eliminate the notorious effect of Li^+ ions. Recently, CO_2 doping was developed to oxidize the Spiro-OMeTAD precursor solution

and reduce the density of Li$^+$ ions in the HTL.[25] Unfortunately, most of these advances bring the benefit of improved device stability at the cost of sacrificing PCE. The progress in boosting the long-term stability of PSCs lags far behind the rapid increase in PCE. Thus, there is an urgent need to minimize the negative effects of dopants while maintaining device performance. Developing a simple yet efficient method to solve these problems is expected but now it remains challenging.

Here, we demonstrate a phase transfer catalyzed method for LiTFSI doping in Spiro-OMeTAD to improve the stability of PSCs. The modified composition in Spiro-OMeTAD precursor solution is superior to the conventional recipe in following aspects. First, 12-crown-4 as a lithium ionophore can selectively bond with Li$^+$ ions through coordination and promote the dissolution of LiTFSI in CB without requiring acetonitrile. Second, the crowned Li$^+$ ions with a larger size and mass become less active and more difficult to migrate, in turn posing a lowered threat to the device stability. Third, Li(12-crown-4)$^+$ complexes can passivate the defects and reduce the charge recombination both at the interface and in the bulk. The optimized Spiro-OMeTAD precursor enables PSCs to deliver a PCE approaching 23%, compared to 22.28% for the control device. The stability of PSCs is significantly improved due to crowning Li$^+$ ions in the HTL with an increased resistance toward moisture and decreased Li$^+$ ion migration. The phase transfer catalyzed LiTFSI doping can also be applied on π-conjugated polymer HTL, showing a universal application.

Results

Phase transfer catalyzed LiTFSI doping in Spiro-MeOTAD. The sandwich structure of PSCs with LiTFSI doped Spiro-OMeTAD as the HTL is shown in Fig. 1a. The components in conventional precursor solution include Spiro-OMeTAD, LiTFSI, acetonitrile, 4-tert-Butylpyridine (TBP), and CB, in which TBP assists a uniform dispersion of LiTFSI. The related molecule structures are provided in Fig. 1b. LiTFSI as an ionic compound has low solubility in CB (Fig. 1c). Crown ether possesses a specific charge distribution and cavity size that can bind alkali-metal cation with a fitted size through host-guest assembly. Particularly, 12-crown-4 has an interior cavity diameter that matches well with Li$^+$ ion size.[26] In this study, it was chosen to promote the dissociation of LiTFSI and increase the solubility through the following coordination reaction: LiTFSI+12-crown-4→Li(12-crown-4)$^+$+TFSI$^-$. After adding 12-crown-4, LiTFSI can be dissolved quickly in CB and we successfully prepared transparent precursor solution without requiring acetonitrile. For simplicity, the precursor solution (HTL or PSCs) prepared with conventional or modified recipe are denoted as control and target precursor (HTL or PSCs), respectively, in the following discussion unless otherwise stated.

According to electrospray ionization-mass spectrometry (ESI-MS), amass/charge ratio (m/e) of 136.1 that is indicative of H(TBP)$^+$ can be detected in the control precursor but the signal of Li(TBP)$_4^+$ is not present (Fig. 1d), which implies easy desolvation between Li$^+$ ions and TBP. An extra intense peak with a m/e of 183.1 assigned to Li 12-crown-4)$^+$ is found in the target precursor, confirming the specific coordinating reaction.[27] The interaction between 12-crown-4 and Li$^+$ ion was further characterized by

nuclear magnetic resonance (NMR) and Fourier transform infrared spectroscopy (FTIR). Compared with the mixed solution without LiTFSI (acetonitrile+12-crown-4), a positive ^{1}H NMR chemical shift of 12-crown-4 after being combined with Li^{+} ion is identified for the mixture with LiTFSI (Fig. 1e), which suggests a strong Li-O solvation.[28,29] Both the ^{1}H NMR spectra have an intense peak at 1.99 ppm characteristic of the H atoms in acetonitrile. A similar shift can also be observed in the FTIR spectra (Supplementary Fig. 1), validating the formation of crown ether-Li^{+} complex.

Notably, the control and target precursor exhibit a slight different color (Supplementary Fig. 2) and absorption pattern (Fig. 1f).The difference is caused by the change in the Li^{+} ion solvation after modifying the precursor recipe. A schematic drawing that depicts the Li^{+} ion solvation shell is shown in the inset. We studied the solvation energy of Li^{+} ions with first-principal calculations (Supplementary Fig. 3 and Supplementary Note 1). In the control precursor, four TBP molecules surrounding a Li^{+} ion is most favorable from the perspective of energy reduction and a stable solvation shell consequently forms. The Li[+] ion solvation in the target precursor, however, is different. Li^{+} ion can tightly bond with 12-crown-4 with a strong bonding and the crowned Li^{+} ion can further interact with a TBP molecule which will be discussed later. As a consequence of less anchoring sites available, there will be more free TBP molecules that can induce Spiro-OMeTAD de-doping because of the chemical reaction with oxidized Spiro-OMeTAD.[30]

Both the absorption spectra and the conductivity measurement (Fig. 1g and Supplementary Note 2) certify that the modification toward the HTL recipe will not greatly affect the generation of oxidized species and the charge transport. We further monitored the time-dependant change in the PL spectra of unoxidized HTLs in ambient air (Fig. 1h). Pristine Spiro-OMeTAD under UV excitation emits intense blue light with an emission peak around 420 nm while p-type doping results in photoluminescence (PL) quenching.[25] The PL intensity of both the HTLs gradually decrease as the exposure time, a phenomenon of doping in progress. The decrease in PL intensity is nearly in step with each other, proving a negligible impact of 12-crown-4 on the oxidation rate of Spiro-OMeTAD. Ultraviolet photoelectron spectroscopy (UPS) of the oxidized HTLs was measured to study the energy band structure (Supplementary Fig. 4). The two HTLs after oxidation show only a small difference in the energy band position and work function, which suggests a similar p-type doping level regardless of the HTL composition.

Elucidation of doping mechanism. To deepen our perception about the role of 12-crown-4 in the doping process, cyclic voltammetry (CV) was conducted to study the oxygen redox couple in LiTFSI-containing electrolyte without or with 12-crown-4. The CV curve without 12-crown-4 has an obvious oxidation peak of O_2^{2-} at 0.01 V while no oxidation peak of O_2^- can be found (Fig. 2a and Supplementary Note 3).[31] This proves that O_2^- has converted into O_2^{2-} during the cathodic sweeping. According to the hard-soft-acid-base theory,[32] the hard Li^{+} ions have a higher affinity for hard Lewis bases such as O_2^{2-} and O^{2-} than moderately soft base (O_2^-). LiO_2 is quite unstable and it appears as an intermediate phase. However, after adding 12-crown-4, an oxidation peak at -0.40 V increase remarkably and the oxidation peak of O_2^{2-}

declines. The extra oxidation peak is assigned to the oxidation reaction from O_2^- to O_2,[33] which confirms the existence of O_2^- and a strong interaction between O_2^- and the crown ether-Li^+ complexes. The Lewis acidity of Li^+ ion is decreased with an increased radius through coordinating with 12-crown-4. As a result, the moderately soft base O_2^- will have an increased affinity for the $Li(12$-crown-$4)^+$ complexes.[33,34] The addition of 12-crown-4 can substantially improve the stability of the O_2^- ions and inhibit the formation proportion of Li_2O_2.

^7Li NMR spectra of the precursor solutions before and after conducting O_2-bubbling (Fig. 2b) were measured to further clarify the difference between the two HTLs in the oxidation process. The O_2-bubbling process is an effective method to pre-oxidize HTL precursor solution. The control and target HTL precursor without pre-oxidization has a peak around -0.85 ppm and -0.78 ppm, respectively. A positive chemical shift in the ^7Li NMR spectra suggests a different coordination condition for Li^+ ion due to the formation of crown ether-Li^+ complexes in the target HTL precursor solution.[26] This phenomenon is in agreement with the result of ^1H NMR as discussed above. After O_2-bubbling, the dominating peak position remains almost the same for the control precursor and the signal at the positive side slightly increases, which is due to the formation of Li_2O_2 that contains Li vacancies.[33] The ^7Li NMR signal of the target precursor shifts to -0.97 ppm after pre-oxidization. We speculate that this change is attributed to the replacement of TBP with O_2^- as the ligand for the crowned Li^+ ion. In lithium oxides, the ^7Li NMR peak position follows the order: $LiO_2<Li_2O_2<Li_2O$ and the peaks at lower frequencies can be assigned to Li species with a higher coordination number.[35,36] The oxidation induced chemical shift is consistent with the enhanced coordination number for Li^+ ions after the bonding between O_2^- and the crowned Li^+ ion.

To get an in-depth understanding of the molecular interaction at the nanoscale, we calculated the binding energy of involved configurations (Fig. 2, c-e) by first-principal calculations. The binding energy for Li^+ ion and 12-crown-4 complexation is -4.23 eV. Such a high binding energy ensures the stable existence of the $Li(12$-crown-$4)^+$ complex. The system energy decreases by -1.28 eV when the crowned Li^+ ion further interact with a TBP molecule, suggesting Li^+ ions in the target precursor exist most likely in the form of $Li(12$-crown-$4)^+$TPB complex. When the ligand of the crowned Li^+ ion is substituted with O_2^-, the decrease in energy can reach up to -5.15 eV. Therefore, O_2^- can bond with crowned Li^+ ion more tightly than TBP molecule and supports our speculation that the crowned Li^+ ion will be finally stabilized with O_2^- after O_2-bubbling.

In the control HTL, lithium oxides including Li_2O_2 and Li_2O eventually form after the oxidative reaction (Fig. 2f, Supplementary Note 4).[9] Lithium oxides are extremely hygroscopic and can easily react with moisture to form lithium hydroxide.[37, 38] It is one of the main reasons for the instability of Spiro-OMeTAD based HTL and will be discussed later. In the target HTL, Li^+ ions are crowned by 12-crown-4 and the direct reaction with oxygen-reduction species is postponed, leaving less opportunity for the generation of lithium oxides. The crowned Li^+ ion with a decreased Lewis acidity has a strong interaction with the

moderately soft base O_2^- as confirmed by the calculations and C-V analyses, so they can be stabilized in the final HTL. At this point, the oxidation mechanism of the p-type doping in the target HTL is straightforward and the involved oxidation process is presented in Fig. 2g.

Charge dynamics and photovoltaic performance. Both the control and target HTLs deposited on perovskite films are compact according to the scanning electron microscope (SEM) and atomic force microscope (AFM) images (Supplementary Fig. 5). The perovskite/HTL films have quenched PL intensity compared with the pristine perovskite film and the one with a target HTL display a little stronger PL intensity than that with a control HTL (Fig. 3a). The time-resolved PL (TRPL) spectra (Supplementary Fig. 6) can be divided and fitted into two parts (Supplementary Table 1). With the existence of HTL, the fast process (τ_1) relates to the charge extraction and the slow one (τ_2) represents the radiative recombination.[39] The perovskite film with a target HTL has a lower τ_1 and higher τ_2. We conclude that the target HTL possesses a better capability in extracting charge carriers from perovskite[40] and the charge recombination is decreased for perovskite film with a target HTL. The lifetime decay behavior is in connection with the crown ether-Li$^+$ complexes (Supplementary Fig. 7 and Supplementary Note 5), which can passivate the perovskite and reduce charge recombination.[29] The defect passivation will exert a positive influence on the device performance.[41] In addition, we measured the space charge limited current (SCLC) of the HTLs (Fig. 3b and Supplementary Note 6) and the defect state density in the target HTL is lower than that in the control HTL.

We fabricated PSCs with a regular-type structure of ITO/SnO$_2$/perovskite/HTL/Ag to investigate the photovoltaic performance (Fig. 3c). The perovskite layer has a bandgap of 1.56 eV. The control PSCs exhibit a PCE of 22.28% with an open-circuit voltage (V_{OC}) of 1.10 V, a short-circuit current density (J_{SC}) of 24.76 mA cm^{-2}, and a fill factor (FF) of 81.74%. In contrast, the target solar cell reached a V_{OC} of 1.10 V, a J_{SC} of 24.98 mA cm^{-2}, and an FF of 83.20%, yielding a PEC of 22.90%. The statistic distributions of photovoltaic parameters based on 25 individual devices for each condition (Fig. 3d, Supplementary Fig. 8) claim that J_{SC} and V_{OC} are slightly influenced by the changed HTL, and the improvement in PCE is mainly attributed to the enhancement in FF. We further evaluated the hysteresis behavior of the PSCs using the two types of HTLs and both the devices suffered from a similar degree of hysteresis (Supplementary Fig. 9). We also systematically investigated the effect of different types of crown ether and the concentration of 12-crown-4 as well as LiTFSI on the photovoltaic performance. The results can be found in the Supplementary Table 2-4.

Crowning lithium ions improves device stability. To evaluate the stability of the perovskite films at the presence of HTL, as-prepared perovskite films with different HTLs were stored in an ambient condition with a humid of around 40%. The fresh samples are dark in color (Fig. 4a). After aging for 550 h, the perovskite film with a control HTL turns yellow while the one with a target HTL still keeps a dark color. To obtain more insights into the degradation, we measured the XRD patterns of the sample before and after aging (Fig. 4b). Regarding the perovskite film with a control HTL, the signal from PbI$_2$ increases markedly

and an extra peak appears at 11.6° resulting from δ-phase perovskite,[42] which indicates a severe degradation of perovskite caused by the moisture. Conversely, the PbI_2 content of the perovskite film with a target HTL holds constant and the δ-phase has not formed during aging, suggesting a better resistance toward the moisture. The change in nanoscale morphology by comparing the cross-sectional SEM images between the fresh and aged samples[43] and the water contact angle of the HTLs (Supplementary Fig. 10, 11) further illustrate the better moisture stability of the target HTL.

We then explored the Li^+ ion distribution in the PSCs by measuring time-of-flight secondary ion mass spectrometry (ToF-SIMS). ToF-SIMS depth profiles and corresponding 3D mapping are provided in Fig. 4c-4f. In both the PSCs Li^+ ion concentration does not obey a simple Fickian diffusion distribution and there is a higher concentration in the SnO_2 layer than that in the perovskite layer. This suggests a lower affinity of Li^+ ions to perovskite than SnO_2. The same trend of Li^+ ion distribution had been reported in previous literature.[44,45] For the control device, a much higher Li^+ ion signal at the SnO_2 layer than that at the HTL can be found, suggesting a rather serious Li^+ ion migration. In sharp contrast, Li^+ ions primarily located within the target HTL and a relatively small portion of Li^+ ions are diffused out and detected at the SnO_2 layer, indicating the ion migration has been greatly suppressed.[17] The Li^+ ion signal intensity over the perovskite range in the target device is a little higher than that for the control, which is due to the migration of Li(12-crown-4)$^+$ complexes into the inner part of perovskite film where the 12-crown-4 has a high affinity to Li^+ ions.

To assess the moisture stability of the resultant PSCs, we traced the photovoltaic performance during storing the unencapsulated devices in the dark at 25 $^\circ$C and 30% relative humidity. The target device maintains 95% of initial PCE after aging over 2000 h, whereas a significant degradation in PCE with only 67% initial value being preserved after 1400 h occurs for the control device (Fig. 4g). The thermal stability of control and target PSCs were compared with unencapsulated devices aged at 60 $^\circ$C in a glove box. The target device shows a much slower decrease in PCE than the control device and 90% of initial PCE can be maintained after thermal aging for 700 h (Supplementary Fig. 12). The lowered Li^+ ion diffusivity in the target HTL due to a strong complexation of the Li^+ ion with 12-crown-4 contributes to a higher degree of thermal stability. These results fully demonstrate that the stability of the target solar cell is better than that of the control device, which is ascribed to the use of high-quality HTL.

Phase transfer catalyzed doping in π-conjugated polymer. π-conjugated polymers can be also used as HTL for PSCs in spite of less satisfactory performance compared with Spiro-OMeTAD. Finally, we performed phase transfer catalyzed LiTFSI doping in poly(3-hexylthiophene-2,5-diyl) (P3HT), a well-known π-conjugated conductive polymer. The addition of 12-crown-4 into the P3HT based HTL precursor also avoid the use of acetonitrile and convert the mobile Li^+ ions into the crown ether-Li^+ complexes. PSCs fabricated using P3HT as the HTL with a phase transfer catalyzed LiTFSI doping exhibit comparable PCE compared with conventional P3HT HTL based device (Supplementary Fig. 13). The P3HT layer with phase transfer catalyzed LiTFSI doping protects the perovskite film from moisture

attacks in humid conditions (Supplementary Fig. 14). The improvement in stability is primarily attributed to the formation of the crown ether-Li$^+$ complexes in the HTL with an enhanced resistance against the moisture.

Discussion

In summary, we have demonstrated the feasibility of phase transfer catalyzed doping in small molecule and conjugated polymer as HTL for stable and high-efficiency PSCs. We show that 12-crown-4 as an efficient phase transfer catalyst can ensure a successful p-type doping and capturing Li ions by forming crown ether-Li$^+$ complexes in the HTL greatly reduces dopant induced side effects such as ion migration, moisture sensitivity, and perovskite layer degradation. This simple but effective doping process can simultaneously improve the photovoltaic performance and long-term stability, which may help pave the way for the commercialization of PSCs in the future. The phase transfer catalyzed doping for organic semiconductor may also find application in other optoelectronic devices by serving as efficient and stable building blocks.

Methods

Materials. Perovskite precursor compounds (formamidinium iodide (FAI, Greatcell Solar), methylammonium bromide (MABr, Xian polymer), methylammonium chloride (MACl, Xian polymer), caesium iodide (CsI, Xian polymer), lead iodide (PbI$_2$, Xian polymer), materials for charge transporting layers (SnO$_2$ (15 wt% colloidal dispersion, Alfa), Spiro-OMeTAD (Xian polymer), P3HT (weight-averaged molecular mass Mw=50,000–70,000, Xian polymer), LiTFSI (99.9%, Xian polymer), 12-crown-4 (99%, TCI)), and solvents (N,N-dimethylformamide (DMF, anhydrous, 99.8%, Sigma-Aldrich), dimethyl sulfoxide (DMSO, anhydrous99%, Sigma-Aldrich), CB (anhydrous, 99.8%, Sigma-Aldrich), acetonitrile (anhydrous, 99.8%, Sigma-Aldrich), TBP (98%, Sigma-Aldrich)) were purchased from the stated chemical suppliers. All the chemicals and reagents were used as received without further purification.

Device fabrication. Patterned ITO substrates were cleaned sequentially with ethanol and deionized water in an ultrasonic system each for 15 min and then dried with high purity N$_2$ gas. After a hydrophilic treatment in a UV cleaner for 10 min, a compact SnO$_2$ layer was deposited by spin coating diluted SnO$_2$ colloid aqueous solution (5 wt%) and heated at 150°C for 30 min. Before transferring into a glove box for perovskite film deposition, the substrates were treated with UV light for 10 min. Perovskite films were deposited using an anti-solvent method. The perovskite precursor solutions (1.3 mol L^{-1}) contained stoichiometric FAI, PbI$_2$, MABr, and CsI in a mixed DMF/DMSO solvent (4:1 v/v). The perovskite solution was spin-coated in a two-step program at 1000 r min^{-1} and 6000 r min^{-1} for 10 s and 20 s, respectively. During the second step, chlorobenzene (100 μL) was quickly poured on the spinning substrate 5 s before the end of the program. An annealing step at 120°C for 20 min was followed to promote the crystallization of perovskite film. The as-prepared perovskite film has a composition of Cs$_{0.05}$FA$_{0.85}$MA$_{0.1}$Pb(I$_{0.97}$Br$_{0.03}$)$_3$. After cooling down, a hole transport layer was spin coated on the

perovskite film at 2000 r min^{-1} for 30 s. Two kinds of HTL precursors were used. For the control HTL deposition, a precursor solution consisted of 72.3 mg Spiro-OMeTAD, 28.8 μL TBP, and 17.5 μL of LiTFSI (520 mgmL^{-1} in acetonitrile) in 1 mL CB. For the target HTL deposition, the components in the precursor solution include 72.3 mg Spiro-OMeTAD, 9 mg LiTFSI, 28.8 μL 4-tert-butyl pyridine, 6 μL12-crown-4, and 1 mL CB. The control P3HT precursor solution contains 20 mg P3HT in 1 mL CB, 7.5 μL TBP and 15 μL LiTFSI solution (170 mg LiTFSI in 1mL acetonitrile), while in the target P3HT precursor solution we added 20 mg P3HT, 7.5 μL TBP, 2.5 mg LiTFSI, and 1.7 μL 12-crown-4 in 1 mL CB. After oxidation overnight, a 90 nm thick Ag film was deposited by thermal evaporation as the back contact. For long-term stability test, 90 nm thick Au film was deposited instead of Ag. The active area is 0.11 cm^2 defined by a shadow mask during thermal evaporation.

Material characterization. ESI-MS was carried out on a high-resolution mass spectrometer (Thermofisher, Q Exactive). The ESI-MS spectra for the control and target HTL precursor were compared. The chemical shift for ^{7}Li NMR was measured with a liquid NMR spectrometer (600M, Bruker avance) and deuterated DMSO was used as the solvent. The control and target HTL precursor solution before and after O$_2$-bubbling were tested. The chemical shift for ^{1}H NMR was measured with a liquid NMR spectrometer (400M, Bruker avance) and deuterated chloroform was used as the solvent. The mixed solution of acetonitrile and 12-crown-4 with and without LiTFSI were tested. The UV-visible spectra were collected by a Shimadzu UV3600 spectrophotometer. FTIR spectra were measured by a Fourier infrared spectrometer (Nicolet 6700, Bruker). Steady-state PL and TRPL spectra were recorded by a spectrofluorometer (Edinburgh, FLS 1000). The XPS spectra were collected using a monochromatic X-ray source on an X-ray photoelectron spectrometer (ESCALAB 250Xi). Cyclic voltammetry was carried out by an electrochemical station (CHI760). The supporting electrolyte contained LiTFSI (0.05 mol L^{-1}) in O$_2$ saturated DMSO. A glassy carbon rotating disc electrode was used as the working electrode. An Ag/Ag$^+$ electrode, immersed in DMSO containing 0.05 mol L^{-1} LiTFSI and 0.005 mol L^{-1} AgNO$_3$, was employed as the reference electrode. The CV curves were recorded at a scan rate of 5 mV s^{-1}. The LiTFSI/DMSO electrolyte with 20 mol% 12-crown-4 (a percentage to the LiTFSI concentration) was chosen to repeat the scan again. The morphology of the samples was characterized by a field-emission scanning electron microscope (SEM, Hitachi, SU8016) and atomic force microscope (AFM, Multimode 8, BRUKER). All the characterizations were measured at room temperature.

Device characterization. Current density-voltage (*J-V*) curves of the perovskite solar cells were measured using a solar simulator under AM 1.5G irradiation and a Keithley 2400 source-meter. The light intensity was calibrated to 100 mW cm^{-2} with a certified reference solar cell (Oriel, 91150V), and the scan range was from 1.2 to 0 V with a delay time of 10 ms. Neither light soaking nor pre-biasing were applied before the *J-V* scan. A non-reflective mask with an aperture size of 0.0625 cm^2 was used to cover the active area of the PSCs to avoid the scattered light and overestimated photocurrent. All the measurements were conducted in an ambient condition (30% relative humidity, 25 °C). For the long-term stability test, PSCs without encapsulation were used. The shelf-life stability was traced by measuring the *J-V* curves of PSCs

at a specific time interval. The devices were stored in an ambient condition (30% relative humidity, 25 °C) for the aging test. For thermal stability test, the devices were aged at a temperature of 60 °C in a glove box full of N_2. TOF-SIMS (Tofsims 5, Iontof) was used to obtain depth profiles and ion distribution in 3D space. The ion depth profiles were measured by sputtering PSCs with a 1 kV O_2 gas gun rastered over a 280×280 μm^2 area followed by probing the composition of the exposed surface with a 30 kV Bi^+ liquid metal ion gun and analyzing positive secondary ions across a 112×112 μm^2 area. The devices were sent out to external labs and the measurements were conducted 48 hours after the fabrication.

Theoretical Calculation. All calculations were done using the Gaussian 16 program. Density functional theory (DFT) calculations with the B3LYP-D3 functional and the 6-311G+(2d,2p) basis set were used to locate all the stationary points involved. The solvation energies of Li^+ ion associated with the formation of $Li^+(TBP)_n$ coordination were calculated according to $\Delta E_{sol}=E[Li^+(TBP)_n]-E[Li^+]-E[(TBP)_n]$, where E is the ab initio total energy of the unit in the brackets, n is the number of coordinating TBP in the solvation sheath of a Li^+ ion. The binding energies for molecular interaction in different configurations: crowned Li^+ ion, crowned Li^+/TBP, and crowned Li^+/O_2^- are calculated in a similar way.

Data Availability

The authors declare that the data supporting the findings of this study are available within the paper and its supplementary materials.

Declarations

Author contributions

K. D. and L. L. conceived the idea. Y. S. and K. D. carried out most of the experiments. Q. C. and G. G. participated in the fabrication of perovskite solar cells. K. D. and L. L. supervised the project and wrote the manuscript. All authors discussed the results.

Competing interests

The authors declare that they have no competing interests.

References

1. Jiang, Q. et al. Surface passivation of perovskite film for efficient solar cells. *Nat. Photon.* **13**, 460–466 (2019).

2. Hui, W. et al. Stabilizing black-phase formamidinium perovskite formation at room temperature and high humidity. *Science* **371**, 1359–1364 (2021).

3. Wang, Y. et al. Thermodynamically stabilized β-CsPbI$_3$-based perovskite solar cells with efficiencies>18%. *Science* **365**, 591–595 (2019).

4. Luo, D. et al. Enhanced photovoltage for inverted planar heterojunction perovskite solar cells. *Science* **360**, 1442–1446 (2018).

5. Lin, R. X. et al. Monolithic all-perovskite tandem solar cells with 24.8% efficiency exploiting comproportionation to suppress Sn(II) oxidation in precursor ink. *Nat. Energy* **4**, 864–873 (2019).

6. Yoo, J. J. et al. Efficient perovskite solar cells via improved carrier management. *Nature* **590**, 587–593 (2021).

7. Leijtens, T. et al. Stability of metal halide perovskite solar cells. *Adv. Energy Mater.* **5**, 1500963 (2015).

8. Jena, A. K., Numata, Y., Ikegami, M. & Miyasaka, T. Role of Spiro-OMeTAD in performance deterioration of perovskite solar cells at high temperature and reuse of the perovskite films to avoid Pb-waste. *J. Mater. Chem. A* **6**, 2219–2230 (2018).

9. Abate, A. et al. Lithium salts as "redox active" p-type dopants for organic semiconductors and their impact in solid-state dye-sensitized solar cells. *Phys. Chem. Chem. Phys.* **15**, 2572–2579 (2013).

10. Zou, J. et al. Solvent engineering of LiTFSI towards high-efficiency planar perovskite solar cells. *Sol. Energy* **194**, 321–328 (2019).

11. Dawson, J. A. et al. Mechanisms of lithium intercalation and conversion processes in organic-inorganic halide perovskites. *ACS Energy Lett.* **2**, 1818–1824 (2017).

12. Tan, B. et al. LiTFSI-free Spiro-OMeTAD-based perovskite solar cells with power conversion efficiencies exceeding 19%. *Adv. Energy Mater.* **9**, 1901519 (2019).

13. Xu, B. et al. Tert-butylpyridine free organic hole transporting materials for stable and efficient planar perovskite solar cells. *Adv. Energy Mater.* **7**, 1700683 (2017).

14. Zhao, B. X. et al. A hole-transport material that also passivates perovskite surface defects for solar cells with improved efficiency and stability. *Energy Environ. Sci.* **13**, 4334–4343 (2020).

15. Jeon, N. J. et al. A fluorene-terminated hole-transporting material for highly efficient and stable perovskite solar cells. *Nat. Energy* **3**, 682–689 (2018).

16. Guo, H. et al. A coplanar π-Extended quinoxaline based hole-transporting material enabling over 21% efficiency for dopant-free perovskite solar cells. *Angew. Chem. Int. Ed.* **60**, 2674–2679 (2021).

17. Kim, S. G. et al. Capturing mobile lithium ions in a molecular hole transporter enhances the thermal stability of perovskite solar cells. *Adv. Mater.* **33**, e2007431 (2021).

18. Jeong, M. et al. Stable perovskite solar cells with efficiency exceeding 24.8% and 0.3-V voltage loss. *Science* **369**, 1615–1620 (2020).

19. Jeong, J. et al. Pseudo-halide anion engineering for α-FAPbI$_3$ perovskite solar cells. *Nature*, **592**, 381–385 (2021).

20. Kim, G. et al. Impact of strain relaxation on performance of α-formamidinium lead iodide perovskite solar cells. *Science* **370**, 108–112 (2020).

21. Nguyen, W. H., Bailie, C. D., Unger, E. L. & McGehee, M. D. Enhancing the hole-conductivity of Spiro-OMeTAD without oxygen or lithium salts by using Spiro(TFSI)$_2$ in perovskite and dye-sensitized solar cells. *J. Am. Chem. Soc.* **136**, 10996–11001 (2014).

22. Jeon, I. et al. Lithium-ion endohedral fullerene (Li$^+$@C60) dopants in stable perovskite solar cells induce instant doping and anti-oxidation. *Angew. Chem. Int. Ed.* **57**, 4607–4611 (2018).

23. Zhang, J., Zhang, T., Jiang, L., Bach, U. & Cheng, Y. B. 4-tert-Butylpyridine free hole transport materials for efficient perovskite solar cells: a new strategy to enhance the environmental and thermal stability. *ACS Energy Lett.* **3**, 1677–1682 (2018).

24. Pham, N. D. et al. Alkaline-earth bis(trifluoromethanesulfonimide) additives for efficient and stable perovskite solar cells. *Nano Energy* **69**,104412 (2020).

25. Kong, J. et al. CO$_2$ doping of organic interlayers for perovskite solar cells. *Nature* **594**, 51–56 (2021).

26. Lu, Z. et al. Crowning metal ions by supramolecularization as a general remedy toward a dendrite-free alkali-metal battery. *Adv.Mater.* **33**, 2101745 (2021).

27. Gu, S. et al. Nitrate additives coordinated with crown ether stabilize lithium metal anodes in carbonate electrolyte. *Adv. Funct. Mater.* **31**, 2102128 (2021).

28. Wang, H. et al. Electrolytes enriched by crown ethers for lithium metal batteries. *Adv. Funct. Mater.* **31**, 2002578 (2020).

29. Zhang, H. et al. Multimodal host-guest complexation for efficient and stable perovskite photovoltaics. *Nat. Commun.* **12**, 3383–3383 (2021).

30. Lamberti, F. et al. Evidence of Spiro-OMeTAD de-doping by tert-butylpyridine additive in hole-transporting layers for perovskite solar cells. *Chem* **5**, 1806–1817 (2019).

31. Wang, X. C. et al. Influence of 12-Crown-4 on oxygen electrode of aprotic Li-O$_2$ battery. *Acta Phys. Chim. Sin.* **32**, 343–348 (2016).

32. Pearson, R. G. Hard and soft acids and bases. *J. Am. Chem. Soc.* **85**, 3533–3539 (1963).

33. Gao, X., Chen, Y., Johnson, L. & Bruce, P. G. Promoting solution phase discharge in Li-O$_2$ batteries containing weakly solvating electrolyte solutions. *Nat. Mater.* **15**, 882–888 (2016).

34. Lopez, N. et al. Reversible reduction of oxygen to peroxide facilitated by molecular recognition. *Science* **335**, 450–453 (2012).

35. Lyu, Z. et al. Promoting defective-Li$_2$O$_2$ formation via Na doping for Li-O$_2$ batteries with low charge overpotentials. *J. Mater. Chem. A* **7**, 10389–10396 (2019).

36. Zhu, Z. et al. Anion-redox nanolithia cathodes for Li-ion batteries. *Nat. Energy* **1**, 16111 (2016).

37. Laoire, C., Mukerjee, S., Abraham, K., Plichta, E. & Hendrickson, M. Influence of nonaqueous solvents on the electrochemistry of oxygen in the rechargeable lithium-air battery. *J. Phys. Chem. C* **114**, 9178–9186 (2010).

38. Aetukuri, N. B. et al. Solvating additives drive solution-mediated electrochemistry and enhance toroid growth in non-aqueous Li-O_2 batteries. *Nat. Chem.* **7**, 50–56 (2015).

39. Wu, Z. et al. Highly efficient perovskite solar cells enabled by multiple ligand passivation. *Adv. Energy Mater.* **10**, 1903696 (2020).

40. Wang, R. et al. Constructive molecular configurations for surface-defect passivation of perovskite photovoltaics. *Science* **366**, 1509–1513 (2019).

41. Zheng, X. et al. Defect passivation in hybrid perovskite solar cells using quaternary ammonium halide anions and cations. *Nat. Energy* **2**, 17102 (2017).

42. Liu, Y. et al. Stabilization of highly efficient and stable phase-pure $FAPbI_3$ perovskite solar cells by molecularly tailored 2D-overlayers. *Angew. Chem. Int. Ed.* **59**, 15688–15694 (2020).

43. Lee, I., Yun, J., Son, H. & Kim, T. Accelerated degradation due to weakened adhesion from Li-TFSI additives in perovskite solar cells. *ACS Appl. Mater. Interfaces* **9**, 7029–7035 (2017).

44. Li, Z. et al. Extrinsic ion migration in perovskite solar cells. *Energy Environ. Sci.* **10**, 1234–1242 (2017).

45. Ding, C. et al. Synergetic effects of electrochemical oxidation of Spiro-OMeTAD and Li^+ ion migration for improving the performance of n-i-p type perovskite solar cells. *J. Mater. Chem. A* **9**, 7575–7585 (2021).
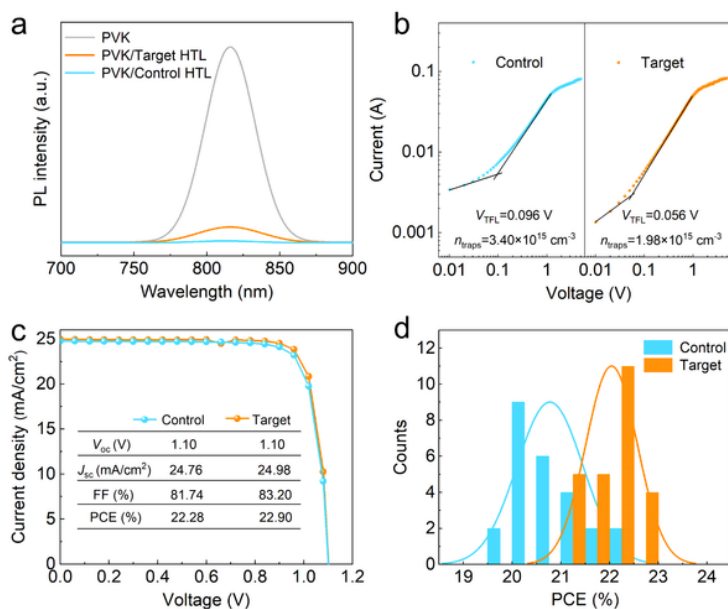
Figures
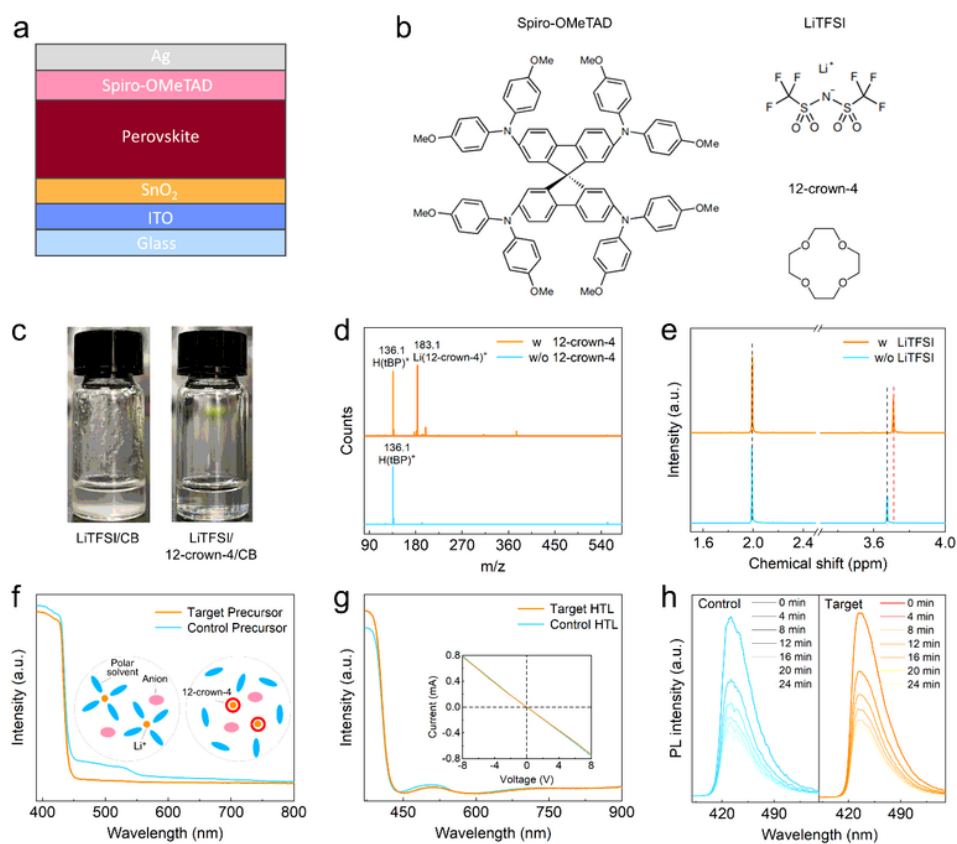
Figure 1

Characterization for phase transfer catalyzed LiTFSI doping in Spiro-OMeTAD. a An schematic architecture of regular-type PSCs. b Molecular structures of Spiro-OMeTAD, LiTFSI , and 12-crown-4. c Optical images showing the dissolution of LiTFSI in CB without and with 12-crown-4. d ESI-MS spectra of control and target precursor solutions. e 1H NMR spectra of 12-crown-4 and acetrolline mixture without and with LiTFSI. f Absorption spectra of precursor solutions. Inset schematically depicts the Li+ ion solvation shell in control (left) and target (right) precursor. g Absorption spectra of HTLs. Inset shows the I-V curves for conductivity measurement. h Time-dependant PL intensity of unoxidized HTLs exposed in air.
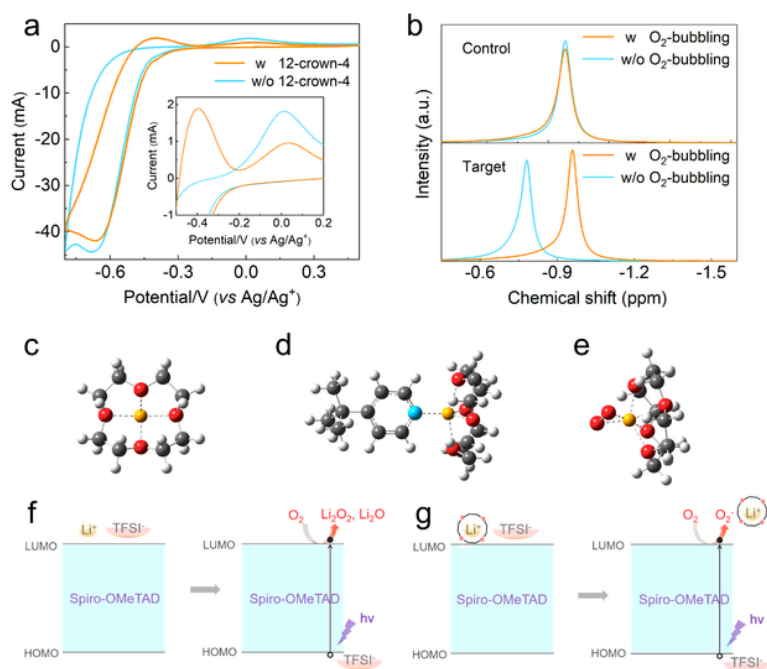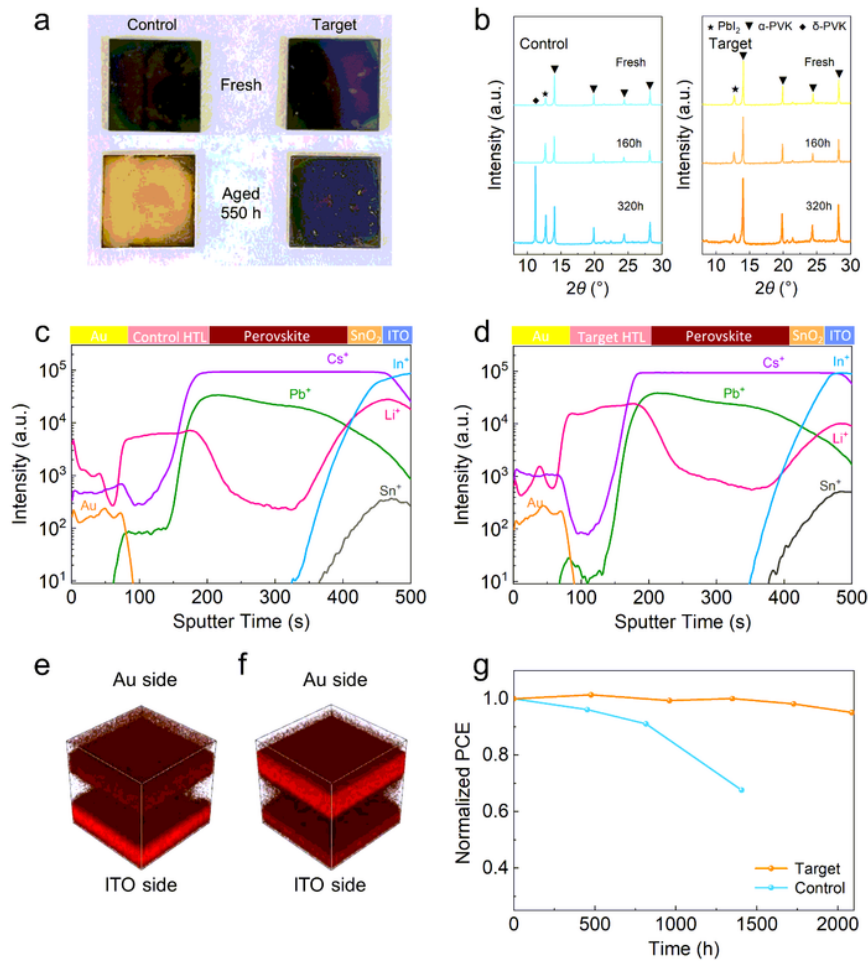
Figure 2

Spiro-OMeTAD oxidation mechanism. a CV scan of LiTFSI-DMSO electrolyte without and with 12-crown-4. The oxidation peaks are zoomed in the inset. b 7Li NMR spectra of precursor solution before and after O2-bubbling. Molecular interaction in different configurations: c crowned Li+ ion, d crowned Li+/TBP, e crowned Li+/O2-. Schematic drawing showing the oxidation mechanism in f control and g target HTL.

Figure 3

Charge dynamics and photovoltaic performances. a PL spectra of perovskite, perovskite with control HTL, and perovskite with target HTL. b SCLC of HTLs. c J-V curves of typical PSCs. d Statistic distribution of PCE.

Figure 4

Stability of films and PSCs. a Optical images and b XRD patterns of perovskite films with control and target HTLs before and after aging in air with 40% RH for a different period. ToF-SIMS depth profiles and 3D Li+ mapping of c e control and d f target PSCs. g Shelf stability of PSCs aged in 30% RH ambient air at 25 oC.

Supplementary Files

This is a list of supplementary files associated with this preprint. Click to download.

- Supplementarymaterials.docx